Visualizing Dynamics of Sub-Hepatic Distribution of Nanoparticles Using Intravital Multiphoton Fluorescence Microscopy

Shih-Hsun Cheng,[†,||,▼] Feng-Chieh Li,[§,▼] Jeffrey S. Souris,[⊥] Chung-Shi Yang,[‡] Fan-Gang Tseng,[||] Hsuan-Shu Lee,[¶] Chin-Tu Chen,[⊥] Chen-Yuan Dong,[§,#,△,]* and Leu-Wei Lo[†,]*

[†]Division of Medical Engineering Research and [‡]Center for Nanomedicine Research, National Health Research Institutes, Zhunan, Miaoli 350, Taiwan, [§]Department of Physics, National Taiwan University, Taipei 106, Taiwan, [⊥]Department of Radiology, The University of Chicago, Chicago, Illinois 60637, United States, [||]Institute of NanoEngineering and MicroSystems, National Tsing Hua University, Hsinchu 300, Taiwan, and [¶]Institute of Biotechnology, [#]Center for Quantum Science and Engineering, and [△]Biomedical Molecular Imaging Core, Division of Genomic Medicine, Research Center for Medical Excellence, National Taiwan University, Taipei 100, Taiwan. [▼]These authors contributed equally to this work.

At present, there is considerable interest in the use of targeted nanoparticles for the detection and treatment of human diseases. Their unique, easily manipulated, size dependency results in the creation of a wide variety of novel structures with unique physical and chemical properties.[1−6] Emerging studies, however, suggest that a number of their unique attributes are likely to give rise to acute and chronic toxic sequelae, a situation further compounded by the typically inefficient targeting and inherently high stability that many nanomaterials exhibit *in vivo*.[7−13] While a variety of schemes have been devised to minimize deleterious side effects (*e.g.*, coating nanoparticles with polymers/ antioxidants/surfactants/ligands or altering nanoparticle size/shape/roughness/surface charge[13−18]), such measures often only partially ameliorate the toxicity of the nanoparticles and can themselves have undesired consequences (*e.g.*, increasing a nanoparticle's hydrodynamic diameter that then results in its substantially altered biodistribution). Correlation of nanoplatform design with its targeting kinetics and therapeutic efficacy thus requires the microscopic knowledge of dynamic nanoparticle distribution in biological systems.
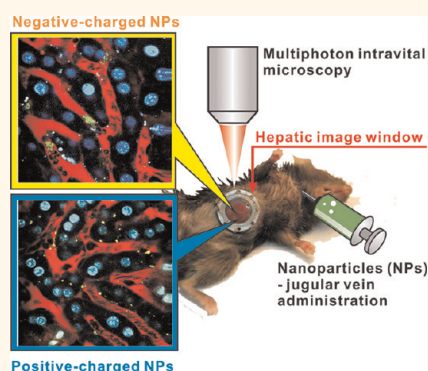
From existing clearance/excretion studies, it is known that, when delivered intravenously, nanoparticle uptake occurs by one of five pathways: phagocytosis, macropinocytosis, caveolin-mediated, clathrin-mediated, and caveolin/ clathrin-indpendent endocytosis, and the processing rate of these nanoparticles largely depends on the particle's hydrophobicity, surface charge, and size.[13,16,17,19−26] Hydrophobic nanoparticles are rapidly removed from circulation by components of the reticuloendothelial system (RES), in particular, by the liver and spleen. As a result, these structures have short *in vivo* half-lives (from seconds to minutes) that often limit their clinical utility and can lead to hepatotoxicity. Nanoparticles that carry significant

ABSTRACT Nanoparticles that do not undergo renal excretion or *in vivo* degradation into biocompatible debris often accumulate in the reticuloendothelial system, also know as the mononuclear phagocyte system, with undesired consequences that limit their clinical utility. In this work, we report the first application of intravital multiphoton fluorescence microscopy to dynamically track the hepatic metabolism of nanoparticles with subcellular resolution in real time. Using fluorescently labeled mesoporous silica nanoparticles (MSNs) in mice as a prototypical model, we observed significant hepatocyte uptake of positively charged, but not negatively charged, moieties. Conversely, *in vivo* imaging of negatively charged, but not positively charged, MSNs reveals an overwhelming propensity for the former's rapid uptake by Kupffer cells in liver sinusoids. Since the only prerequisite for these studies was that nanoparticles are fluorescently labeled and not of a specific composition or structure, the techniques we present can readily be extended to a wide variety of nanoparticle structures and surface modifications (*e.g.*, shape, charge, hydrophobicity, PEGylation) in the preclinical assessment and tailoring of their hepatotoxicities and clearances.

KEYWORDS: reticuloendothelial system · intravital multiphoton fluorescence microscopy · mesoporous silica nanoparticles · Kupffer cells · surface modifications

surface charge tend to adsorb serum proteins (some in non-native conformation) that can affect their biodistribution, elicit immune response, and indiscriminately destabilize cell membranes and proteins. Furthermore, nanoparticle size strongly correlates with clearance route, with particles 3 nm in diameter and smaller extravasating tissues nonspecifically, those 3–8 nm in diameter undergoing renal clearance, 30–80 nm nanoparticles being sequestered in lung and leaky vasculature (e.g., tumor and inflamed tissue, via the enhanced permeation and retention effect), and particles larger than 80 nm becoming trapped by liver and spleen.[14]

Of course, uptake from circulation does not ensure excretion. Indeed, all studies to date of the larger quantum dots (diameter >8 nm), regardless of surface coating, have shown rapid sequestering by the RES of liver and spleen, but with none ever leaving those organs.[17,21] Similar retention patterns have been observed with pristine single-walled carbon nanotubes, with rapid accumulations in liver, spleen, and lung, but with little subsequent excretion from those organs.[27] To prolong circulation times and avoid rapid hepatic sequestering, polyethylene glycol (PEG) coatings have typically been employed but with mixed, particle-dependent results. Early studies suggested that PEGylated nanoparticles escaped uptake by Kupffer cells in liver and B cells in spleen because their PEG chains partially blocked serum protein adsorption from nanoparticle surfaces.[28,29] However, recent studies of PEGylated gold nanospheres, with long blood circulation times (~30 h), have demonstrated a propensity to accumulate in the liver and spleen of mice for up to 7 days following injection, leading to acute hepatic inflammation and apoptosis.[9] Torchilin et al. found the net surface charge of PEGylated liposomes, rather than the steric hindrance of PEG chains, to be the key factor affecting their uptake by the RES.[30] Coll et al. reported that hybrid nanoparticles, conjugated with different terminal groups of PEG, present different biodistributions and that those bearing positive end groups (NH_2) strongly favored accumulation in resident, phagocyte-rich tissues.[31]

As nanoparticles that do not undergo renal excretion or in vivo degradation generally accumulate in the liver with undesirable consequences, dynamic microscopic imaging of their fate is crucial to the design and validation of highly targeted, safe nanoplatforms. Recently, intravital fluorescence multiphoton imaging has emerged as a powerful technique for studying cellular level events in vivo,[32–38] including the binding of nanomaterials to tumor vasculature and neovasculature.[39,40] While studies employing whole-body animal imaging techniques have been utilized to visualize the distribution of nanoparticles in vivo,[41–44] these approaches lack the spatial and temporal resolution to follow the dynamics of nanoparticle transport at the single cellular level in vivo. In earlier
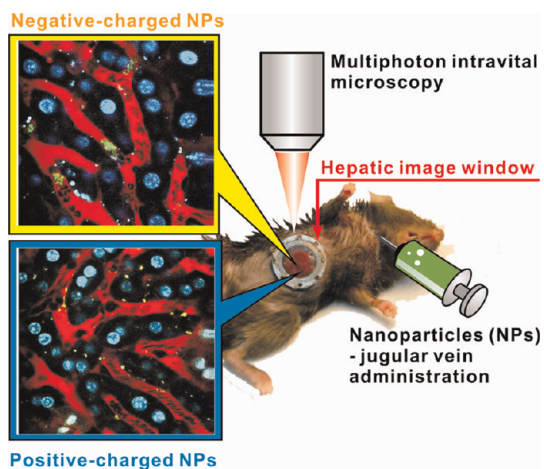
Scheme 1. Multiphoton intravital microscopy visualizes dynamics of sub-hepatic distribution of different surface-charged nanoparticles. We demonstrated the use of in vivo multiphoton imaging to track the hepatic metabolism of nanoparticles in real time at subcellular resolution.

studies of hepatobilliary metabolism, we reported the use of multiphoton fluorescence microscopy to record the intravital dynamics of uptake, processing, and excretion of an organic anion, 6-carboxyfluorescein diacetate (6-CFDA), in mice.[45] In the current work, we demonstrated the use of in vivo multiphoton imaging to track, for the first time, the hepatic metabolism of nanoparticles in real time at subcellular resolution (Scheme 1).

RESULTS AND DISCUSSION

For these investigations, we elected to use MCM-41 mesoporous silica nanoparticles (MSNs). With its intrinsically large surface area (~1000 m^2/g), large pore volume (~1.0 cm^3/g), inherent chemical stability, and highly ordered hexagonal pore structure and adjustable pore size (1.5–10 nm), MCM-41 mesoporous silica has been used in a variety of applications including catalysis,[46–48] drug delivery,[49–53] and controlled drug release.[54–58] Earlier studies have shown that these nanoparticles are noncytotoxic and well suited for the efficient and protective transport of lipid-insoluble molecules across cell/organelle membranes.[55–60] Slowing et al. described various surface functionalizations of MCM-41 MSNs, and their effect upon cell uptake by HeLa cells in serum-free media as a positive correlation between uptake and net surface charge was found.[61] In addition, Chung et al. reported similar uptake/surface charge correlation of MSNs in human fibroblast cells (3T3-L1) and human mesenchymal stem cells (hMSCs).[62] However, to the best of our knowledge, in vivo visualization of the hepatobiliary processing of surface-charge-modified, silica-based nanoparticles in the RES has not been achieved.

We synthesized fluorescently labeled mesoporous silica nanoparticles (MSNs) using conventional sol–gel chemistry, with extraction of surfactant templates in warm, acidic ethanol.[63] Fluorescein isothiocyanate

TABLE 1. Characterization of Different Surface Charges of FITC-MSNs

samples	$S_{BET}{}^a$ (m^2/g)	$W_{BJH}{}^a$ (nm)	zeta-potential ζ^b (mV)	isoelectric point[b]	particle size via TEM (nm)	particle size via DLS[b] (nm)
FITC-MSN	1020	2.5	−12.0	6.9	100 ± 10	132.8
FITC-MSN-1X	950	2.4	+26.0	8.5	100 ± 10	160.4
FITC-MSN-3X	860	2.2	+45.0	10.1	100 ± 10	162

[a] Nitrongen adsorption—desorption measurments were made on a Micromertics ASAP 2020 at 77 K. Surface area and pore size determinations were obtained using Brunauer—Emmett—Teller (BET) and Barrett—Joyner—Halenda (BJH) methods, respectively. [b] Zeta-potential and hydrodynamic radius of FITC-MSNs (suspended in DI, pH 7.4) were obtained via a Malvern Zetasizer.
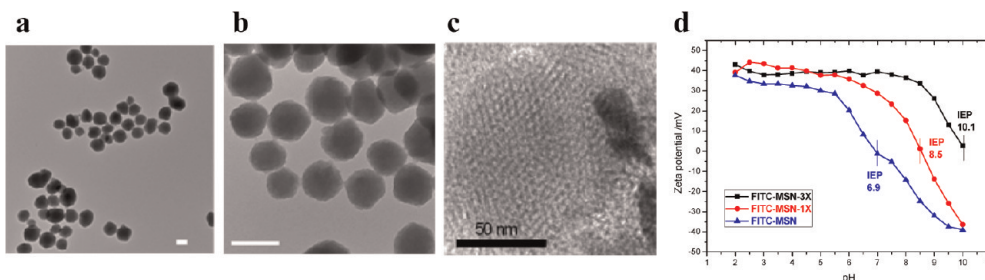

Figure 1. Characteristics of FITC-MSN samples. (a−c) TEM images showing the characteristic hexagonal structure of FITC-MSN samples (scale bar: (a,b) 100 nm and (c) 50 nm). (d) Zeta-potential dependence on pH for various MSN constructs, with mean values listed at the isoelectric point.

(FITC) was selected as the fluorophore for multiphoton tracking as it can be excited by the two-photon process. Furthermore, FITC can be protected from photobleaching and O_2 quenching by the MSNs' silica framework. MSN surface charge modifications were made during particle synthesis via varying the concentration of 3-aminopropyltrimethoxysilane (APTMS) present during postmodification (refer to the Materials and Methods section). In this manner, three unique moieties, FITC-MSN (unmodified), FITC-MSN-1X (modified with 1 equivalent concentration of APTMS), and FITC-MSN-3X (modified with 3 equivalent concentration of APTMS), can be produced. Morphologies of the final MSN constructs were characterized by transmission electron microscopy (TEM), dynamic light scattering (DLS), N_2 adsorption—desorption isotherm measurement, and zeta-potential measurement (Table 1).

TEM showed uniform, well-dispersed, hexagonal MSNs with average particle diameters of ∼100 nm (Figure 1a−c). N_2 adsorption—desorption isotherm measurements of the various nanoplatforms (Table 1) revealed type IV behavior characteristic of highly uniform, cylindrical pore geometries, with decreased nanoparticle surface areas for increased amino group labeling. Specifically, we used the Brunauer—Emmett—Teller (BET) method, and it was determined that the surface areas were 1020 m^2/g for FITC-MSN, 950 m^2/g for FITC-MSN-1X, and 860 m^2/g for FITC-MSN-3X. Similarly, average pore size for the various constructs decreased with increased amino group conjugation. For pore size determination, the Barrett—Joyner—Halenda (BJH) method was used and it was found that the pore sizes were 2.5 nm for FITC-MSN, 2.4 nm for FITC-MSN-1X, and 2.2 nm for FITC-MSN-3X.

Zeta-potential measurements of FITC-MSN, FITC-MSN-1X, and FITC-MSN-3X were also made via automated titration in aqueous (deionized) solutions, with pH values ranging from 2 to 10 (Figure 1d). The zeta-potentials at physiological pH (7.4) of −12.0/+26.0/+45.0 mV correspond to negative/moderately positive/highly positive net surface charge, and isoelectric points at pH 6.9/8.5/10.1 were recorded for FITC-MSN/FITC-MSN-1X/FITC-MSN-3X constructs, respectively. Dynamic light scattering studies demonstrated polydispersity indexes (PDI) of all MSN samples to be below 0.1 (data not shown) and hydrodynamic radii of 132.8 nm for FITC-MSN, 160.4 nm for FITC-MSN-1X, and 162.0 nm for FITC-MSN-3X at pH 7.4.

Prior to in vivo application, functionalized MSNs were incubated with human hepatoma cells (HepG2) in 5% FBS for 0.5, 1.0, and 2.0 h. Cells were then imaged for localization with confocal microscopy and in order to characterize the functionalized MSNs' in vitro uptake efficiency, cellular fluorescence quantified via flow cytometry. Whereas negatively charged (unmodified) FITC-MSNs demonstrated low uptake efficiency in HepG2 cells even after 1 or 2 h of incubation (Figure 2a,d), positively charged FITC-MSN-1X (Figure 2b,e) and FITC-MSN-3X (Figure 2c,f) showed a nearly 10-fold greater, time-dependent percentage uptake for all incubation periods (Figure 2g).

For real-time intravital multiphoton microscopy, the mouse was first surgically implanted with a hepatic imaging chamber held in registration via a U-shaped, grooved steel plate that directly attached to the specimen stage of the imaging microscope. The multiphoton imaging instrument used in this study has been described previously.[64] In short, the 780 nm output of a
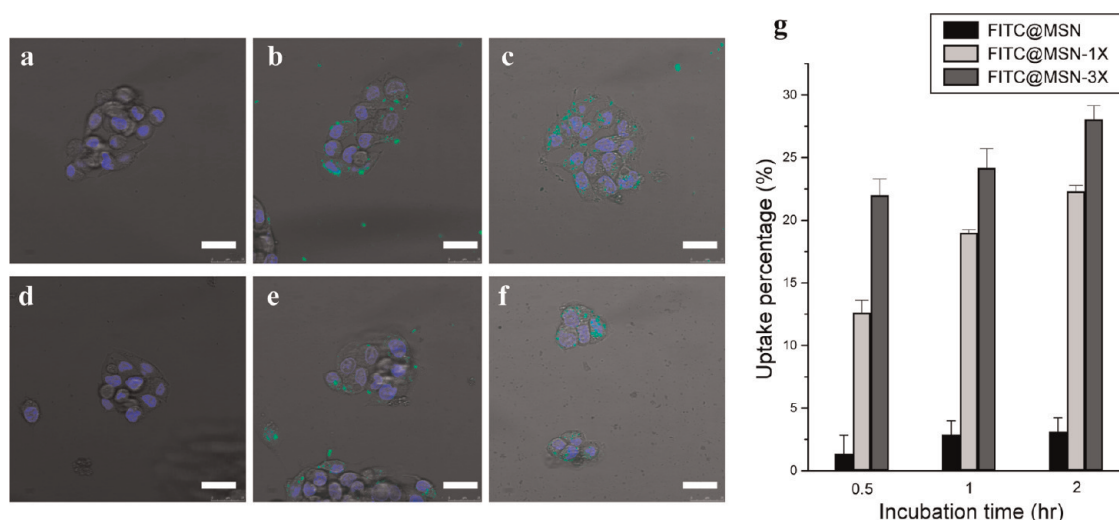
Figure 2. *In vitro* uptake efficacy of FITC-MSN samples in cultured HepG2 cells. Merged confocal and DIC images of the cellular uptake of (a) FITC-MSN, (b) FITC-MSN-1X, and (c) FITC-MSN-3X after 1 h incubation (green pseudocolor, fluorescence of FITC-MSNs; blue pseudocolor, Hoechst 33342 labeled nuclei). Merged confocal and DIC images of the cellular uptake of (d) FITC-MSN, (e) FITC-MSN-1X, and (f) FITC-MSN-3X after 2 h incubation (scale bars: 50 μm). (g) Uptake percentage of various FITC-MSN constructs for 0.5, 1.0, and 2.0 h incubation with hepatocytes, as determined by flow cytometry (n = 3 for each incubation).
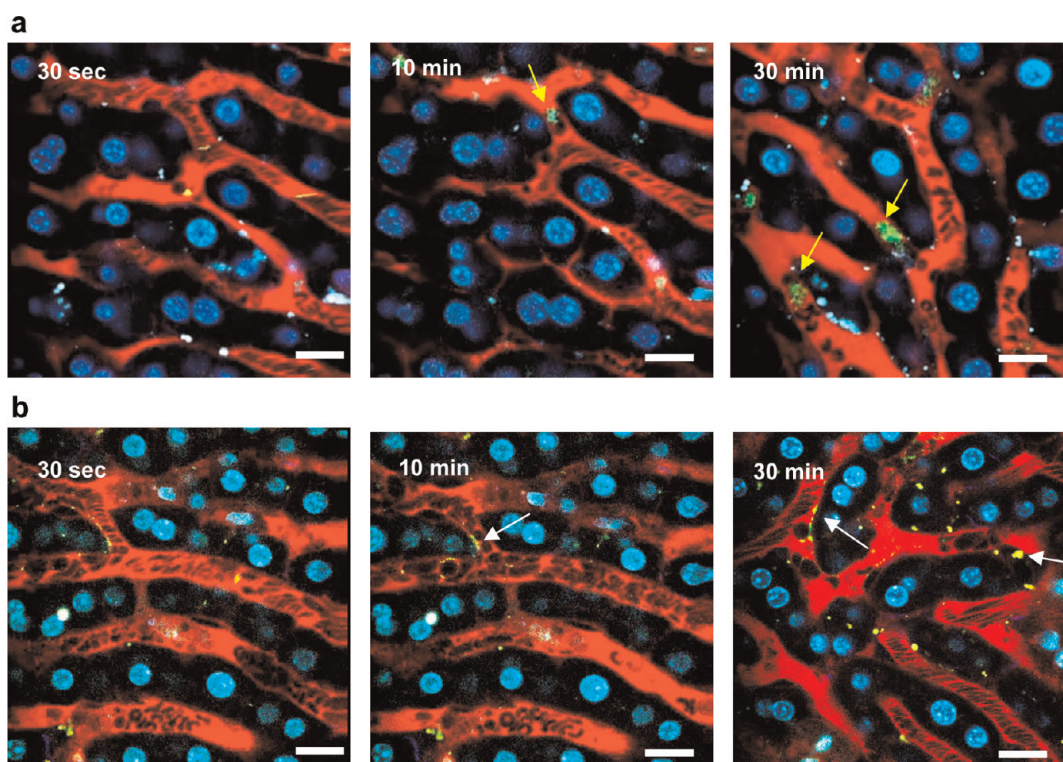

Figure 3. Real-time hepatic visualization of negatively and positively charged FITC-labeled MSNs (frame captures from Supporting Information movies S1 and S2). Time-lapsed multiphoton images acquired approximately 30 μm below the capsule. Time (in minutes) indicates period postinjection of (a) FITC-MSN (yellow arrows) and (b) FITC-MSN-3X (white arrows) (scale bars: 50 μm). Images were merged from three channels. Red: rhodamine/dextran R6G (MW 70 000) staining of sinusoids. Green: fluorescence of FITC-MSNs. Blue: hepatocyte nuclei labeled with Hoechst 33342.

titanium:sapphire laser (Tsunami, Spectra Physics, Mountain View, CA) pumped by a diode-pumped solid-state laser (Millennia X, Spectra Physics) was used as the excitation source. The laser source was guided into a home-modified inverted microscope (TE2000, Nikon, Tokyo, Japan) by a galvanometer-driven, $x-y$ mirror scanning system (model 6220, Cambridge Technology, Lexington, MA). Upon entering the microscope, a high numerical aperture, oil-immersion objective (S Fluor 40×, NA 1.3, Nikon) was used for
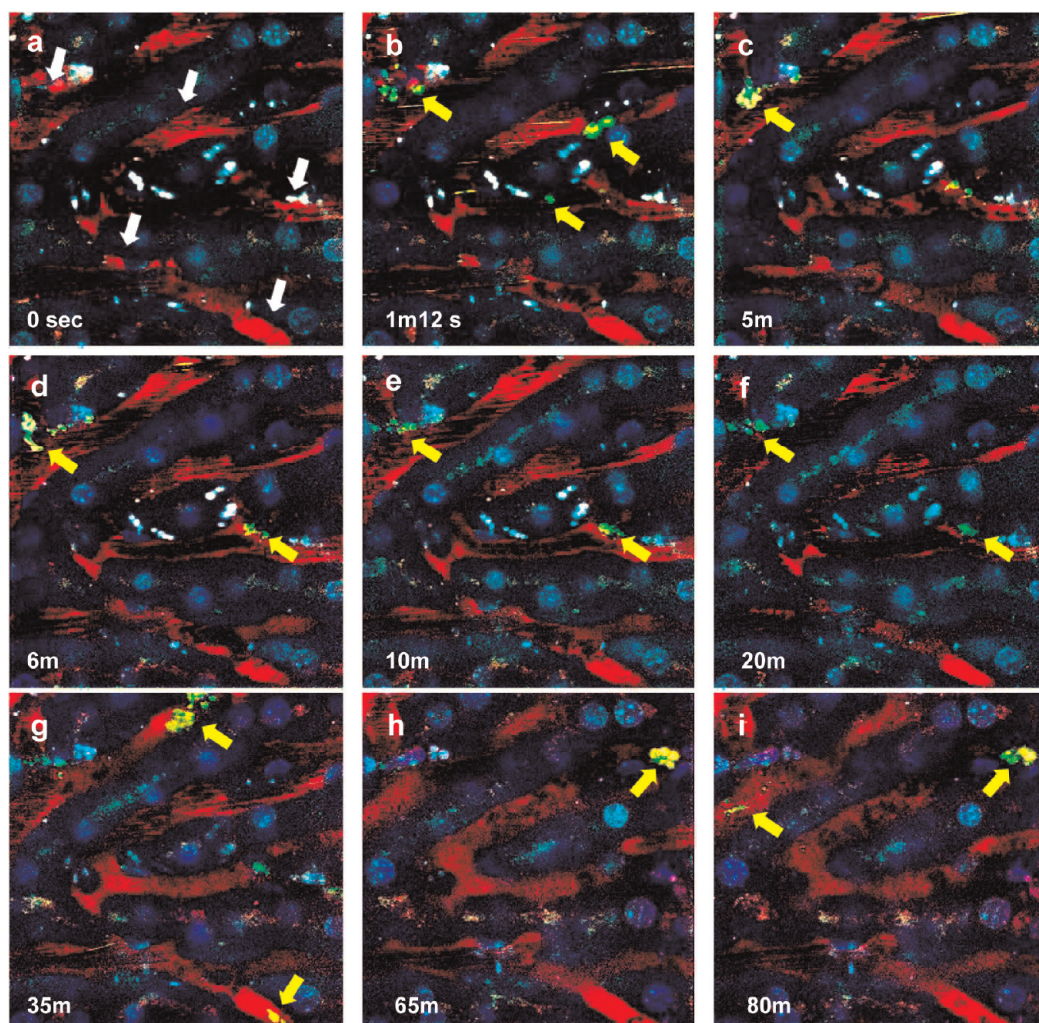
Figure 4. Direct hepatic images of FITC-MSNs of negative surface charge, captured by Kupffer cells. (a−i) Time-lapsed multiphoton images acquired approximately 30 μm below the capsule. Time (in minutes) indicates period postinjection of negatively charged FITC-MSN. Images were merged from three channels. Red: PE-labeled F4/80 antibody staining of Kupffer cells (white arrows). Green: fluorescence of FITC-MSNs. Blue: hepatocyte nuclei labeled with Hoechst 33342. Yellow arrows indicate co-registration of FITC-MSNs with Kupffer cells.

focusing the excitation source onto the mouse liver *in vivo*. The fluorescence and second harmonic generation signals were then collected in the epi-illuminated or backscattered geometry and further processed by additional dichroic mirrors (435DCXR, 495DCXR, 555DCLP, Chroma Technology, Rockingham, VT) and band-pass filters (HQ390/20, HQ460/50, HQ525/50, HQ590/80, Chroma Technology) into four detection channels. The respective detection bandwidths of the channels were 390 ± 10, 460 ± 25, 525 ± 25, and 590 ± 40 nm for the detection of second harmonic generation (SHG), blue, green, and red fluorescence, respectively.

In order to inject fluorescent MSNs and other labeling molecules, an indwelling catheter (PE-10) was inserted into the right jugular vein for direct injection. The sinusoids were visualized with rhodamine B isothiocyanate/dextran 70000, and the cell nuclei were marked with Hoechst 33342. Time-lapsed multiphoton

imaging commenced as quickly as FITC-MSNs were intravenously injected at a concentration of 16 mg/kg through the jugular vein. The images were acquired at 4 s intervals, and Image J (National Institute of Health, Bethesda, MD) and MetaMorph (Universal Imaging, Downingtown, PA) were used to postprocess the acquired images. Figure 3 shows the time course of MSN hepatic trafficking in mice that had been injected with negatively charged FITC-MSN (Figure 3a, Supporting Information movie S1) and positively charged FITC-MSN-3X (Figure 3b, Supporting Information movie S2). In the frame captures, blood vessels are denoted by their labeling with rhodamine B isothiocyanate/dextran MW 70 000 (red channel), cell nuclei are denoted by their staining with the dye Hoechst 33342 (blue channel), and the FITC-MSNs are denoted by their intrinsic fluorescence (green channel).

Initially, nanoparticle transit times in the microscope's field of view were brief and the localized
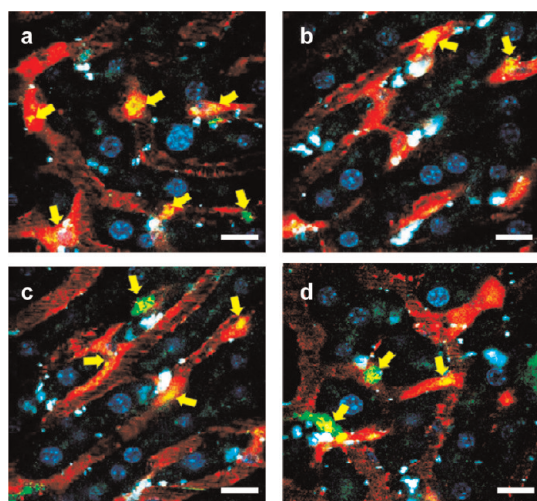
Figure 5. Hepatic images of FITC-MSN with negative surface charge 2 h postinjection. (a–d) Kupffer cells reveal significant capture of FITC-MSNs (yellow arrows indicate co-registration of FITC-MSNs with Kupffer cells. Red: PE-labeled F4/80 antibody staining of Kupffer cells. Green: fluorescence of FITC-MSNs. Blue: hepatocyte nuclei labeled with Hoechst 33342 (scale bars: 50 μm).

MSN number densities small such that no MSNs were observed. Approximately 10 min postinjection, negatively charged FITC-MSNs (Figure 3a, middle) began to aggregate in the sinusoids. After 30 min, significant aggregations of the negatively charged FITC-MSNs became evident within blood vessels (Figure 3a, right). No aggregation of positively charged FITC-MSN-3X nanoparticles in hepatic blood vessels was observed (Figure 3b). However, followed by trespass from sinusoids, substantial endocytic accumulation of FITC-MSN-3X nanoparticles within hepatocytes in parenchyma was observed 30 min following their injection (see Supporting Information movie S2), possibly due to apolipoprotein E and IgA binding-enhanced uptake. In Figure 3a,b, the imaging regions are the same at 30 s and 10 min, respectively. By contrast, the different regions of imaging shown at 30 min were selected to

illustrate that the MSN sub-hepatic distributions are consistent in regions other than the originally selective ones.

We postulated that the aggregation of negatively charged FITC-MSNs in hepatic blood vessels arose first from the binding of serum proteins[19] to the nanoparticles, followed by their opsonin-mediated uptake by macrophages lining the walls of the sinusoids. In previous reports, Gessner et al. demonstrated that negatively charged polystyrene nanoparticles (PS) of 100 nm in diameter absorb about twice as much protein as positively charged PS.[65] Additionally, they used 2D protein gel electrophoresis to indicate that the IgG immunoglobulins are the major protein group found on the surface of these particles.[65] Recently, Lunov et al. reported that macrophages internalized 4 times more negatively charged PS than THP-1 monocytic cells when analyzed in serum-containing medium.[66] In addition, the intravenously applied negatively charged PS were found predominantly accumulating in the chicken liver, where macrophages of the RES reside.[66]

To test this hypothesis, we labeled Kupffer cells in situ with PE-labeled F4/80 antibodies as shown in Figure 4 (red color). Two hours after in situ Kupffer cell staining, FITC-MSN nanoparticles were intravenously injected via the jugular vein and multiphoton imaging commenced. As expected, and shown in Figure 4, negatively charged fluorescent nanoparticles colocalized with the labeled Kupffer cells in a time-dependent manner. First, significant accumulations of the fluorescent MSNs were observed in Kupffer cells within 60 min of their injection. Two hours following their injection, the concentrations of FITC-MSNs within Kupffer cells continued to grow (Figure 5a–d). No Kupffer cell uptake of positively charged MSNs, either FITC-MSN-1X or FITC-MSN-3X, was observed. Sequestering of positively charged MSNs by hepatocytes and negatively charged MSNs by Kupffer cells was confirmed via TEM of excised tissues (Figure 6).
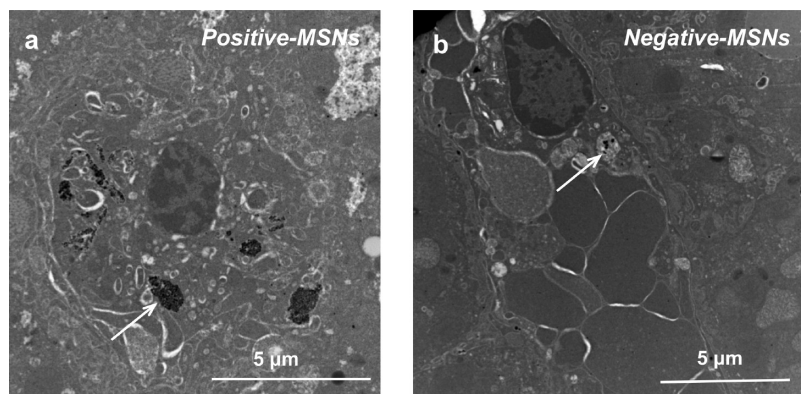

Figure 6. TEM images of sub-hepatic distribution of MSNs with positive and negative net surface charge. (a) Typical TEM image of hepatocyte with white arrow showing the late endosome/lysosome-encapsulated MSNs of net positive surface charge. **(b)** TEM image of Kupffer cell that resides on the endothelium of the sinusoid. White arrow indicates the Kupffer cell bearing MSNs of net negative surface charge.

CONCLUSION

In this work, we reported the first application of intravital multiphoton fluorescence microscopy to dynamically track the hepatic metabolism of nanoparticles with subcellular resolution in real time. Compared to conventional confocal fluorescence microscopy, the longer excitation wavelength used in multiphoton imaging results in reduced photodamage and prolonged observation. These advantages are invaluable for the real-time imaging of nanoplatform deposition *in vivo*. In this study, we elected to use mesoporous silica nanoparticles as the prototypical nanoplatform due to its growing employment in drug delivery, the robustness and photostability of the imbedded fluorophore, and the ease with which their surface charge can be modified. Intravital real-time imaging of fluorescently labeled MSNs in mice demonstrated significant hepatocyte uptake of positively charged, but not negatively charged, moieties. This observation was confirmed by TEM of excised tissues and

in vitro by confocal microscopy following nanoparticle incubation with human hepatocytes. Conversely, *in vivo* imaging of negatively charged, but not positively charged, MSNs revealed an overwhelming propensity for the former's rapid uptake by Kupffer cells in liver sinusoids, a finding also consistent with TEM of excised tissues and *in vitro* by confocal microscopy following nanoparticle incubation with human Kupffer cells. However, unlike the uptake of positively charged MSNs by hepatocytes, which have the potential for host clearance *via* hepatobiliary excretion, negatively charged MSNs' accumulation in Kupffer cells portends significant hepatoxicity. Since the only prerequisite for these studies was that nanoparticles be fluorescently labeled and not of a specific composition/structure, the techniques we present can readily be extended to a wide variety of nanoparticles with different surface modifications (*e.g.*, shape, charge, hydrophobicity, PEGylation) in the preclinical assessment and tailoring of their hepatotoxicities and clearances.

MATERIALS AND METHODS

Materials. Tetraethoxysilane (TEOS), cetyltrimethylammonium bromide (CTAB), ethanol, ammonium hydroxide (30%), *N,N*-dimethylformamide (DMF), and 3-aminopropyltrimethoxysilane (APTMS) were purchased from Acros. Fluorescein isothiocyanate (FITC), rhodamine B isothiocyanate/dextran 70000, and Hoechst 33342 were obtained from Sigma Chemical Co. Mouse F4/80 labeled with phycoerythrin (PE-labeled F4/80 antibodies) was purchased from BioLegend.

Synthesis of FITC-MSN Samples. The FITC-conjugated APTMS was synthesized by stirring FITC (2 mg) with APTMS/EtOH solution (0.1 M in 10 mL of ethanol) in darkness for 24 h. Separately, CTAB (0.58 g) was dissolved in NH_4OH (0.51 M, 300 mL) at 40 °C and then added to a dilute solution of TEOS (0.2 M in 5.0 mL of ethanol), followed by vigorous stirring for 5 h. The above FITC-APTMS solution (5.0 mL) and TEOS (1.0 M in 5.0 mL of ethanol) were then mixed together with vigorous stirring for another 1 h. The resulting solution was then aged at 40 °C for 24 h. Solid samples were collected *via* centrifuging at 12 000 rpm for 20 min, washing, and redispersing the precipitate with deionized water and ethanol several times. To modify different amounts of amino groups on the surfaces of MSNs, we dispersed 200 mg of FITC-MSNs (before extraction) in toluene and added 20 and 60 μL of APTMS (1 mL, 95%) with vigorous stirring to yield FITC-MSN-1X and FITC-MSN-3X, respectively. The mixture solution was then aged at 60 °C for 24 h. Solid samples were collected *via* centrifuging at 12 000 rpm for 20 min, washing, and redispersing the precipitate with deionized water and ethanol several times. Surfactant templates were removed by extraction in acidic ethanol warmed to 65 °C (1 g of HCl in 50 mL of ethanol) over 24 h.

MSN Characterization. The morphology of MSN samples was characterized *via* TEM (Hitachi, H-7650), operating at an acceleration voltage of 80 kV. Surface areas and pore sizes were determined by N_2 adsorption−desorption isotherm measurements at 77 K on a Micrometric ASAP 2010. Samples were outgassed at 10^{-3} Torr and 120 °C for approximately 6 h prior to conduct adsorption experiments. Pore size distribution curves were obtained from analysis of the desorption portion of the isotherms using the BJH (Barrett−Joyner−Halenda) method. Flow cytometry was performed using FACS Calibur flow cytometer (BD Bioscience). A Malvern ZetaSizer Nano was used to measure the zeta-potential, polydispersity, and hydrodynamic diameter of MSN samples in solution at pH 7.4. Zeta-potential

distributions were obtained by averaging 10 measurements. The samples were prepared at a concentration of 2 mg in 1 mL of ddH_2O. The pH values were adjusted by the addition of HCl or NaOH (0.02 M). Before each measurement, each sample was sonicated for 1 min to preclude aggregation.

Cellular Uptake of MSNs. For determination of cellular uptake of FITC-MSNs with positive/negative surface charges, 1×10^6 HepG2 hepatoma cells were plated on 10 cm dishes and incubated for 24 h at 37 °C and 5% CO_2. Cells were then exposed to 50 μg mL^{-1} of either FITC-MSN, FITC-MSN-1X, and FITC-MSN-3X in 10% FBS serum medium and incubated for various times of 0.5, 1.0, and 2.0 h at 37 °C. All treated cells were then washed twice with PBS, trypsinized, and analyzed by flow cytometry. For confocal imaging, 2×10^4 HepG2 cells were cultured in 35 mm μ-Dish (Ibidi, Munich) for 1 day followed by exposure to 50 μg mL^{-1} of either FITC-MSN, FITC-MSN-1X, or FITC-MSN-3X in 10% FBS serum medium for 1 and 2 h at 37 °C. Cells were then washed twice and stained with Hoechst 33342 dye (excitation 350 nm, emission 460 nm) to label cell nuclei for confocal fluorescence microscopy.

Animal Experimental Procedures. C57BL/6 mice beyond 5 weeks of age were obtained from Laboratory Animal Center, National Taiwan University College of Medicine. The mice were anesthetized by intraperitoneal injection of 2−2−2 tribromoethanol (0.35 mg/g body weight) and installed with a hepatic imaging window on the upper abdomen as previously described.[1] They recovered awaiting imaging experiments the next day. This liver surface area served for image acquisition through multiphoton microscopy.

Multiphoton Microscopy. The settings of the multiphoton microscope were as previously described.[64] A titanium:sapphire laser with 780 nm output (Tsunami, Spectra-Physics, Mountain View, CA) pumped by a diode-pumped solid-state laser (Millennia X, Spectra-Physics) was used for excitation. The laser beam was scanned by an $x-y$ mirror scanning system (model 6220, Cambridge Technology, Lexington, MA) and guided toward the modified inverted microscope (TE 2000, Nikon, Tokyo, Japan). Then the laser beam was focused *via* an objective (SFluor 40×, NA 1.3, Nikon) into the sample *in vivo*. Finally, the emission was collected in the epi-illuminated or backscattering geometry and then separated into four simultaneous detection channels by serial dichroic mirrors (435DCXR, 495DCXR, 555DCLP, Chroma Technology, Rockingham, VT) and additional band-pass filters (HQ390/20, HQ460/50, HQ525/50, HQ590/80, Chroma Technology). For nanoparticle injection, an indwelling

catheter (PE-10) was inserted into the right jugular vein and the body stretched out from the posterior neck right before imaging experiments. After the mouse was fixed on the stage, rhodamine B isothiocyanate/dextran 70000 (10 mg/mouse) was injected intravenously for labeling vessels and the cell nuclei were marked with Hoechst 33342 (50 μL of 5 mg/mL). The labeling would persist for longer than 5 h (personal observations), and thus the vascular patterns were always used as landmarks. Time-lapsed multiphoton imaging commenced 2 min after FITC-MSNs were intravenously injected at a concentration of 16 mg/kg of normal saline through the jugular vein. The depth of the imaging area is ∼30 μm under the liver capsule. Fluorescence images were acquired on the fixed microscopic areas serially at 4 s intervals. Zero time was almost prior to FITC-MSN injection. The fluorescence signals at ∼420−470, ∼500−550, and ∼550−630 nm were recorded. They were then pseudocolored into blue, green, and red, respectively. Image J software (National Institute of Health, Bethesda, MD) and MetaMorph (Universal Imaging, Downingtown, PA) were used for image processing. To confirm the Kuppfer cell uptake, we labeled Kuppfer cells *in situ* with PE-labeled F4/80 antibodies (10 μL of 0.2 mg/mL, red color) and the hepatic cell nuclei were marked with Hoechst 33342. Two hours after *in situ* Kuppfer cell staining, FITC-MSN nanoparticles were intravenously injected *via* the jugular vein and multiphoton imaging commenced. The procedures of animal experiments were approved by the Institutional Animal Care and Use Committee, National Taiwan University College of Medicine.

TEM Imaging of Liver Tissues. Sequestering of positively charged MSNs by hepatocytes and negatively charged MSNs by Kuppfer cells was confirmed *via* TEM of excised tissues 2 h postinjection. For electron microscopy, tissue specimens were fixed overnight in glutaraldehyde buffered (2.5%) with phosphate buffered saline (PBS; 0.1 M, pH 7.4). Tissues were then washed three times in PBS and postfixed for 1 h in a solution containing OsO_4 buffered (2%) with PBS. Next, tissues were washed three times in dH_2O and dehydrated stepwise in EtOH. Tissues were polymerized using Spurr resin at 68 °C for 15 h. The embedded specimens were subsequently thin-sectioned into 70 nm slices and viewed on a Hitachi H-7650 TEM, operating at 80 kV.

REFERENCES AND NOTES

1. Loo, C.; Lowery, A.; Halas, N. J.; West, J; Drezek, R. Immunotargeted Nanoshells for Integrated Cancer Imaging and Therapy. *Nano Lett.* **2005**, *5*, 709–711.

2. Brannon-Peppas, L.; Blanchette, J. O. Nanoparticle and Targeted Systems for Cancer Therapy. *Adv. Drug Delivery Rev.* **2004**, *56*, 1649–1659.

3. Davis, M. E.; Chen, Z.; Shin, D. M. Nanoparticle Therapeutics: An Emerging Treatment Modality for Cancer. *Nat. Rev. Drug Discovery* **2008**, *7*, 771–782.

4. Nie, S. M.; Xing, Y.; Kim, G. J.; Simons, J. W. Nanotechnology Applications in Cancer. *Annu. Rev. Biomed. Eng.* **2007**, *9*, 257–288.

5. Penn, S. G.; He, L.; Natan, M. J. Nanoparticles for Bioanalysis. *Curr. Opin. Chem. Biol.* **2003**, *7*, 609–615.

6. Cheon, J.; Lee, J. H. Synergistically Integrated Nanoparticles as Multimodal Probes for Nanobiotechnology. *Acc. Chem. Res.* **2008**, *41*, 1630–1640.

7. Hardman, R. A Toxicologic Review of Quantum Dots: Toxicity Depends on Physicochemical and Environmental Factors. *Environ. Health Perspect.* **2006**, *114*, 165–172.

8. Cheng, C.; Müller, K. H.; Koziol, K. K.; Skepper, J. N.; Midgley, P. A.; Welland, M. E.; Porter, A. E. Toxicity and Imaging of Multi-Walled Carbon Nanotubes in Human Macrophage Cells. *Biomaterials* **2009**, *30*, 4152–4160.

9. Cho, W. S.; Cho, M.; Jeong, J.; Choi, M.; Cho, H. Y.; Han, B. S.; Kim, S. H.; Kim, H. O.; Lim, Y. T.; Chung, B. H.; *et al.* Acute Toxicity and Pharmacokinetics of 13 nm-Sized PEG-Coated Gold Nanoparticles. *Toxicol. Appl. Pharmacol.* **2009**, *236*, 16–24.

10. Bharti, B.; Meissner, J.; Findenegg, G. H. Aggregation of Silica Nanoparticles Directed by Adsorption of Lysozyme. *Langmuir* **2011**, *27*, 9823–9833.

11. Li, C.; Liu, H.; Sun, Y.; Wang, H.; Guo, F.; Rao, S.; Deng, J.; Zhang, Y.; Miao, Y.; Guo, C.; *et al.* PAMAM Nanoparticles Promote Acute Lung Injury by Inducing Autophagic Cell Death through the Akt-TSC2-Mtor Signaling Pathway. *J. Mol. Cell Biol.* **2009**, *1*, 37–45.

12. Ballou, B.; Ernst, L. A.; Andreko, S.; Harper, T.; Fitzpatrick, J. A.; Waggoner, A. S.; Bruchez, M. P. Sentinel Lymph Node Imaging Using Quantum Dots in Mouse Tumor Models. *Bioconjugate Chem.* **2007**, *18*, 389–396.

13. Dobrovolskaia, M. A.; McNeil, S. E. Immunological Properties of Engineered Nanomaterials. *Nat. Nanotechnol.* **2007**, *2*, 469–478.

14. Alexis, F.; Pridgen, E.; Molnar, L. K.; Farokhzad, O. C. Factors Affecting the Clearance and Biodistribution of Polymeric Nanoparticles. *Mol. Pharmaceutics* **2008**, *5*, 505–515.

15. Goel, R.; Shah, N.; Visaria, R.; Paciotti, G. F.; Bischof, J. C. Biodistribution of TNF-α-Coated Gold Nanoparticles in an *In Vivo* Model System. *Nanomedicine* **2009**, *4*, 401–410.

16. Balogh, L.; Nigavekar, S. S.; Nair, B. M.; Lesniak, W.; Zhang, C.; Sung, L. Y.; Kariapper, M. S.; El-Jawahri, A.; Llanes, M.; Bolton, B.; *et al.* Significant Effect of Size on the *In Vivo* Biodistribution of Gold Composite Nanodevices in Mouse Tumor Models. *Nanomedicine* **2007**, *3*, 281–296.

17. Schipper, M. L.; Iyer, G.; Koh, A. L.; Cheng, Z.; Ebenstein, Y.; Aharoni, A.; Keren, S.; Bentolila, L. A.; Li, J.; Rao, J.; *et al.* Particle Size, Surface Coating, and PEGylation Influence the Biodistribution of Quantum Dots in Living Mice. *Small* **2009**, *5*, 126–134.

18. Moghimi, S. M.; Hunter, A. C.; Murray, J. C. Long-Circulating and Target-Specific Nanoparticles: Theory to Practice. *Pharm. Rev.* **2001**, *53*, 283–313.

19. Nel, A. E.; Mädler, L.; Velegol, D.; Xia, T.; Hoek, E. M.; Somasundaran, P.; Klaessig, F.; Castranova, V.; Thompson, M. Understanding Biophysicochemical Interactions at the Nano-Bio Interface. *Nat. Mater.* **2009**, *8*, 543–557.

20. De Jong, W. H.; Hagens, W. I.; Krystek, P.; Burger, M. C.; Sips, A. J.; Geertsma, R. E. Particle Size-Dependent Organ Distribution of Gold Nanoparticles after Intravenous Administration. *Biomaterials* **2008**, *29*, 1912–1919.

21. Choi, H. S.; Liu, W.; Misra, P.; Tanaka, E.; Zimmer, J. P.; Itty Ipe, B.; Bawendi, M. G.; Frangioni, J. V. Renal Clearance of Quantum Dots. *Nat. Biotechnol.* **2007**, *25*, 1165–1170.

22. Sadauskas, E.; Danscher, G.; Stoltenberg, M.; Vogel, U.; Larsen, A.; Wallin, H. Protracted Elimination of Gold Nanoparticles from Mouse Liver. *Nanomedicine* **2009**, *5*, 162–169.

23. Lundqvist, M.; Stigler, J.; Elia, G.; Lynch, I.; Cedervall, T.; Dawson, K. A. Nanoparticle Size and Surface Properties Determine the Protein Corona with Possible Implications for Biological Impacts. *Proc. Natl. Acad. Sci. U.S.A.* **2008**, *105*, 14265–14270.

24. Vertegel, A. A.; Siegel, R. W.; Dordick, J. S. Silica Nanoparticle Size Influences the Structure and Enzymatic Activity of Adsorbed Lysozyme. *Langmuir* **2004**, *20*, 6800–6807.

25. Renaud, G.; Hamilton, R. L.; Havel, R. J. Hepatic Metabolism of Colloidal Gold-Low-Density Lipoprotein Complexes in

the Rat: Evidence for Bulk Excretion of Lysosomal Contents into Bile. *Hepatology* **1989**, *9*, 380–392.

26. Hardonk, M. J.; Harms, G.; Koudstaal, J. Zonal Heterogeneity of Rat Hepatocytes in the *In Vivo* Uptake of 17 nm Colloidal Gold Granules. *Histochemistry* **1985**, *83*, 473–477.

27. Yang, S.-T.; Guo, W.; Lin, Y.; Deng, X.-Y.; Wang, H.-F.; Sun, H.-F.; Liu, Y.-F.; Wang, X.; Wang, W.; Chen, M.; *et al.* Biodistribution of Pristine Single-Walled Carbon Nanotubes *in Vivo. J. Phys. Chem. C* **2007**, *111*, 17761–17764.

28. Aggarwal, P.; Hall, J. B.; McLeland, C. B.; Dobrovolskaia, M. A.; McNeil, S. E. Nanoparticle Interaction with Plasma Proteins as It Relates to Particle Biodistribution, Biocompatibility and Therapeutic Efficacy. *Adv. Drug Delivery Rev.* **2009**, *61*, 428–437.

29. Dobrovolskaia, M. A.; Aggarwal, P.; Hall, J. B.; McNeil, S. E. Preclinical Studies to Understand Nanoparticle Interaction with the Immune System and Its Potential Effects on Nanoparticle Biodistribution. *Mol. Pharmaceutics* **2008**, *5*, 487–495.

30. Levchenko, T. S.; Rammohan, R.; Lukyanov, A. N.; Whiteman, K. R.; Torchilin, V. P. Liposome Clearance in Mice: The Effect of a Separate and Combined Presence of Surface Charge and Polymer Coating. *Int. J. Pharm.* **2002**, *240*, 95–102.

31. Faure, A. C.; Dufort, S.; Josserand, V.; Perriat, P.; Coll, J. L.; Roux, S.; Tillement, O. Control of the *In Vivo* Biodistribution of Hybrid Nanoparticles with Different Poly(ethylene glycol) Coatings. *Small* **2009**, *5*, 2565–2575.

32. Kreisel, D.; Nava, R. G.; Li, W.; Zinselmeyer, B. H.; Wang, B.; Lai, J.; Pless, R.; Gelman, A. E.; Krupnick, A. S.; Miller, M. J. *In Vivo* Two-Photon Imaging Reveals Monocyte-Dependent Neutrophil Extravasation during Pulmonary Inflammation. *Proc. Natl. Acad. Sci. U.S.A.* **2010**, *107*, 18073–18078.

33. Barretto, R. P.; Messerschmidt, B.; Schnitzer, M. J. *In Vivo* Fluorescence Imaging with High-Resolution Microlenses. *Nat. Methods* **2009**, *6*, 511–512.

34. Mark, R. L.; Emily, E. T.; Debasish, S.; Wayne, J. L.; Robb, W. G.; Matthew, F. K. Stabilized Imaging of Immune Surveillance in the Mouse Lung. *Nat. Methods* **2011**, *8*, 91–96.

35. Zoumi, A.; Yeh, A.; Tromberg, B. J. Imaging Cells and Extracellular Matrix *in Vivo* by Using Second-Harmonic Generation and Two-Photon Excited Fluorescence. *Proc. Natl. Acad. Sci. U.S.A.* **2002**, *99*, 11014–11019.

36. Brown, E. B.; Campbell, R. B.; Tsuzuki, Y.; Xu, L.; Carmeliet, P.; Fukumura, D.; Jain, R. K. *In Vivo* Measurement of Gene Expression, Angiogenesis and Physiological Function in Tumors Using Multiphoton Laser Scanning Microscopy. *Nat. Med.* **2001**, *7*, 864–868.

37. Helmchen, F.; Denk, W. Deep Tissue Two-Photon Microscopy. *Nat. Methods* **2005**, *2*, 932–940.

38. Masters, B. R.; So, P. T.; Gratton, E. Multiphoton Excitation Fluorescence Microscopy and Spectroscopy of *In Vivo* Human Skin. *Biophys. J.* **1997**, *72*, 2405–2412.

39. Smith, B. R.; Cheng, Z.; De, A.; Koh, A. L.; Sinclair, R.; Gambhir, S. S. Real-Time Intravital Imaging of RGD-Quantum Dot Binding to Luminal Endothelium in Mouse Tumor Neovasculature. *Nano Lett.* **2008**, *8*, 2599–2606.

40. Smith, B. R.; Cheng, Z.; De, A.; Rosenberg, J.; Gambhir, S. S. Dynamic Visualization of RGD-Quantum Dot Binding to Tumor Neovasculature and Extravasation in Multiple Living Mouse Models Using Intravital Microscopy. *Small* **2010**, *6*, 2222–2229.

41. Ferrari, M. Cancer Nanotechnology: Opportunities and Challenges. *Nat. Rev.* **2005**, *5*, 161–171.

42. Panchapakesan, B.; Wickstrom, E. Nanotechnology for Sensing, Imaging, and Treating Cancer. *J. Surg. Oncol.* **2007**, *16*, 293–305.

43. Veiseh, O.; Sun, C.; Gunn, J.; Kohler, N.; Gabikian, P.; Lee, D.; Bhattarai, N.; Ellenbogen, R.; Sze, A.; Hallahan, A.; *et al.* Optical and MRI Multifunctional Nanoprobe for Targeting Gliomas. *Nano Lett.* **2005**, *5*, 1003–1008.

44. Cheon, J.; Lee, J. H. Synergistically Integrated Nanoparticles as Multimodal Probes for Nanobiotechnology. *Acc. Chem. Res.* **2008**, *41*, 1630–1640.

45. Liu, Y.; Chen, H. C.; Yang, S. M.; Sun, T. L.; Lo, W.; Chiou, L. L.; Huang, G. T.; Dong, C. Y.; Lee, H. S. Visualization of Hepatobiliary Excretory Function by Intravital Multiphoton Microscopy. *J. Biomed. Opt.* **2007**, *12*, 014014.

46. Kesanli, B.; Lin, W. B. Mesoporous Silica Anchored Ru Catalysts for Highly Enantioselective Hydrogenation of β-Ketoesters. *Chem. Commun.* **2004**, *21*, 2284–2285.

47. Wang, Y. J.; Caruso, F. Enzyme Encapsulation in Nanoporous Silica Spheres. *Chem. Commun.* **2004**, *7*, 1528–1529.

48. De Vos, D. E.; Dams, M.; Sels, B. F.; Jacobs, P. A. Ordered Mesoporous and Microporous Molecular Sieves Functionalized with Transition Metal Complexes as Catalysts for Selective Organic Transformations. *Chem. Rev.* **2002**, *102*, 3615–3640.

49. Wang, Y. J.; Bansal, V.; Zelikin, A. N.; Caruso, F. Templated Synthesis of Single Component Polymer Capsules and Their Application in Drug Delivery. *Nano Lett.* **2008**, *8*, 1741–1745.

50. Vallet-Regi, M.; Balas, F.; Arcos, D. Mesoporous Materials for Drug Delivery. *Angew. Chem., Int. Ed.* **2007**, *46*, 7548–7558.

51. Trewyn, B. G.; Slowing, I. I.; Giri, S.; Chen, H. T.; Lin, V. S. Y. Synthesis and Functionalization of a Mesoporous Silica Nanoparticle Based on the Sol−Gel Process and Applications in Controlled Release. *Acc. Chem. Res.* **2007**, *40*, 846–853.

52. Tsai, C. P.; Hung, Y.; Chou, Y. H.; Huang, D. M.; Hsiao, J. K.; Chang, C.; Chen, Y. C.; Mou, C. Y. High-Contrast Paramagnetic Fluorescent Mesoporous Silica Nanorods as a Multifunctional Cell-Imaging Probe. *Small* **2008**, *4*, 186–191.

53. Lu, C. W.; Hung, Y.; Hsiao, J. K.; Yao, M.; Chung, T. H.; Lin, Y. S.; Wu, S. H.; Hsu, S. C.; Liu, H. M.; Mou, C. Y.; *et al.* Bifunctional Magnetic Silica Nanoparticles for Highly Efficient Human Stem Cell Labeling. *Nano Lett.* **2007**, *7*, 149–154.

54. Lu, J.; Choi, E.; Tamanoi, F.; Zink, J. I. Light-Activated Nanoimpeller-Controlled Drug Release in Cancer Cells. *Small* **2008**, *4*, 421–426.

55. Schlossbauer, A.; Kecht, J.; Bein, T. Biotin-Avidin as a Protease-Responsive Cap System for Controlled Guest Release from Colloidal Mesoporous Silica. *Angew. Chem., Int. Ed.* **2009**, *48*, 3092–3095.

56. Meng, H.; Xue, M.; Xia, T.; Zhao, Y. L.; Tamanoi, F.; Stoddart, J. F.; Zink, J. I.; Nel, A. E. Autonomous *In Vitro* Anticancer Drug Release from Mesoporous Silica Nanoparticles by pH-Sensitive Nanovalves. *J. Am. Chem. Soc.* **2010**, *132*, 12690–12697.

57. Lee, C. H.; Cheng, S. H.; Huang, I. P.; Souris, J. S.; Yang, C. S.; Mou, C. Y.; Lo, L. W. Intracellular pH-Responsive Mesoporous Silica Nanoparticles for the Controlled Release of Anticancer Chemotherapeutics. *Angew. Chem., Int. Ed.* **2010**, *49*, 8214–8219.

58. Giri, S.; Trewyn, B. G.; Stellmaker, M. P.; Lin, V. S. Y. Stimuli-Responsive Controlled Release Delivery System Based on Mesoporous Silica Nanorods Capped with Magnetic Nanoparticles. *Angew. Chem., Int. Ed.* **2005**, *44*, 5038–5044.

59. Huang, D. M.; Hung, Y.; Ko, B. S.; Hsu, S. C.; Chen, W. H.; Chien, C. L.; Tsai, C. P.; Kuo, C. T.; Kang, J. C.; Yang, C. S.; *et al.* Highly Efficient Cellular Labeling of Mesoporous Nanoparticles in Human Mesenchymal Stem Cells: Implication for Stem Cell Tracking. *FASEB J.* **2005**, *19*, 2014–2016.

60. Xing, X.; He, X.; Peng, J.; Wang, K.; Tan, W. Uptake of Silica-Coated Nanoparticles by HeLa Cells. *J. Nanosci. Nanotechnol.* **2005**, *5*, 1688–1693.

61. Slowing, I.; Trewyn, B. G.; Lin, V. S. Effect of Surface Functionalization of MCM-41-Type Mesoporous Silica Nanoparticles on the Endocytosis by Human Cancer Cells. *J. Am. Chem. Soc.* **2006**, *128*, 14792–14793.

62. Chung, T. H.; Wu, S. H.; Yao, M.; Lu, C. W.; Lin, Y. S.; Hung, Y.; Mou, C. Y.; Chen, Y. C.; Huang, D. M. The Effect of Surface Charge on the Uptake and Biological Function of Mesoporous Silica Nanoparticles in 3T3-L1 Cells and Human Mesenchymal Stem Cells. *Biomaterials* **2007**, *28*, 2959–2966.

63. Lin, Y. S.; Tsai, C. P.; Huang, H. Y.; Kuo, C. T.; Hung, Y.; Huang, D. M.; Chen, Y. C.; Mou, C. Y. Well-Ordered Mesoporous Silica Nanoparticles as Cell Markers. *Chem. Mater.* **2005**, *17*, 4570–4573.

64. Li, F. C.; Liu, Y.; Huang, G. T.; Chiou, L. L.; Liang, J. H.; Sun, T. L.; Dong, C. Y.; Lee, H. S. *In Vivo* Dynamic Metabolic Imaging of Obstructive Cholestasis in Mice. *Am. J. Physiol.* **2009**, *296*, G1091-7.

65. Gessner, A.; Lieske, A.; Paulke, B. R.; Muller, R. H. Functional Groups on Polystyrene Model Nanoparticles: Influence on Protein Adsorption. *J. Biomed. Mater. Res., Part A* **2003**, *65*, 319–326.

66. Lunov, O.; Syrovets, T.; Loos, C.; Beil, J.; Delacher, M.; Tron, K.; Nienhaus, G. U.; Musyanovych, A.; Mailänder, V.; Landfester, K.; *et al.* Differential Uptake of Functionalized Polystyrene Nanoparticles by Human Macrophages and a Monocytic Cell Line. *ACS Nano* **2011**, *5*, 1657–1669.